Dalton Transactions

Accepted Manuscript

ROYAL SOCIETY OF CHEMISTRY

www.rsc.org/dalton

Ordering effects in the crystal structure and electrochemical properties of the $Gd_{0.5}Ba_{0.5}Mn_{0.5}Fe_{0.5}O_{3-\delta}$ perovskite

Daniel Muñoz-Gil,[a] David Ávila-Brande,[a] Esteban Urones-Garrote [b] and Susana García-Martín [a] *

[a] Departamento de Química Inorgánica, Facultad de C.C. Químicas, Universidad Complutense, 28040-Madrid, Spain.

[b] Centro Nacional de Microscopía Electrónica, Universidad Complutense, E-28040, Madrid, Spain

Abstract

Layered-type ordering and oxygen vacancies ordering are revealed in $GdBaMnFeO_{6-\delta}$ perovskite. Selected area electron diffraction and high-resolution transmission electron microscopy results indicate a modulation of the crystal structure. Ba and Gd ordering in $(001)_p$ layers is confirmed by high angle annular dark field scanning transmission electron microscopy and electron energy-loss spectroscopy. These techniques also revealed formation of layer-stacking defects in the crystals. Direct imaging of the oxygen sublattice is obtained by phase image reconstruction. Location of the oxygen vacancies in the $(GdO)_x$ layers is achieved by analysis of the intensity of the averaged phase image. Physical properties of the $GdBaMnFeO_{6-\delta}$ perovskite, are likely to be strongly affected by its ordering effects and crystal microstructure. In this sense, layered-type $GdBaMnFeO_{6-\delta}$ perovskite show better electrochemical properties as cathodes in SOFCs than ion disordered $Gd_{0.5}Ba_{0.5}Mn_{0.5}Fe_{0.5}O_{3-\delta}$ perovskite.

Introduction

ABO_3 materials with perovskite structure are one of the most important families of complex oxides due to their wide range of properties and applications. Compositional variations in these compounds cause significant modifications of both their crystal and electronic structure, having a great impact in their physical properties. In addition to the flexibility of accommodation of multiple cations onto the A and/or B sites of the structure, ordering effects of the ions and non-stoichiometry can also highly contribute to modifications in the properties of the perovskite-type materials.

In this sense, there is a growing interest in the study of non-stoichiometric perovskites of general formula $A_{1-x}A'_xB_{1-y}B'_yO_{3-\delta}$, where A is a lanthanide atom or Y, A' an alkaline earth and B and B' are transition metal atoms, as electrodes in solid oxide fuel cells (SOFCs) [1,2]. These perovskites are mixed ionic and electronic conductors due to the oxygen anions moving throughout the anion vacancies. Therefore, cation or/and anion vacancies ordering can significantly affect their ion conducting properties. A-cations do preferably adopt layered-type ordering in the perovskite structure. Moreover, in non-stoichiometric perovskites with layered-type ordering such as $GdBaCo_2O_{6-\delta}$, the anion vacancies are expected to mainly locate in particular $(AO)_x$ planes (in the $(GdO)_x$ planes in $GdBaCo_2O_{6-\delta}$) forming very high conducting layers, which increase the oxygen-ion diffusion in comparison with the A-cation disordered perovskites [3,4]. Molecular Dynamic studies in $GdBaCo_2O_{6-\delta}$ suggest that oxygen diffusion occurs only in the $(GdO)_x$ planes and decreases when the Gd and Ba atoms disorder due to the appearance of anion diffusion all over the structure [5]. Further experimental studies in $PrBaCo_2O_{6-\delta}$ also indicate anisotropic oxygen diffusion [6]. The excellent electrochemical behaviour of $GdBaCo_2O_{6-\delta}$ in symmetrical cells using $Ce_{0.8}Gd_{0.2}O_{2-\delta}$ as electrolyte reported back in 2006 [7,8] has developed increasing attention in the study of A-cation ordered perovskites (also called layered-type perovskites) as cathodes for intermediate temperature SOFCs (IT-SOFCs). Layered-type perovskites such as $SmBaCo_2O_{6-\delta}$ [9] and $PrBaCo_2O_{6-\delta}$ [10] have demonstrated high electrocatalytic activity for the oxygen reduction at intermediate temperatures. However, most of these cobaltites are not chemically stable with some important IT-electrolytes such as $La_{1-x}Sr_xGa_{0.8}Mg_{0.2}O_{3-\delta}$ perovskites and have high thermal expansion coefficients. Therefore, new materials are currently being investigated as cathodes for IT-SOFCs. For instance, decreasing of thermal expansion coefficients is found by Fe substitution in $ABaCo_{2-x}Fe_xO_{6-\delta}$ (A = Gd, Pr) perovskites [11,12]. Another interesting example of layered-type perovskite is $PrBaMn_2O_{6-\delta}$, which has also recently be reported as a high-performance anode for SOFCs [13].

We report in this article the synthesis and characterization of A-cation disordered $Gd_{0.5}Ba_{0.5}Mn_{0.5}Fe_{0.5}O_{3-\delta}$ and A-cation ordered $GdBaMnFeO_{6-\delta}$ perovskites and compare their electrochemical performance as cathodes in symmetrical cells using $Ce_{0.9}Gd_{0.1}O_{2-\delta}$ electrolyte. While several Co-based perovskites with A-cation ordering have been

isolated, preparation of Mn-based perovskites requires at least a two-step method and reducing atmosphere [14]. A-cation ordering in $GdBaMnFeO_{6-\delta}$ is achieved by obtaining an oxygen-deficient perovskite with $\delta \sim 1$ under reducing conditions, which can be further oxidized.

We study the ordering effects on the crystal structure of $GdBaMnFeO_{6-\delta}$ by a combination of techniques: selected area electron diffraction (SAED), high-resolution transmission electron microscopy (HRTEM), high angle annular dark field scanning transmission electron microscopy (HAADF-STEM), electron energy-loss spectroscopy (EELS) and exit wave reconstruction (EWR). Instrumental improvements in HRTEM such as reduction of spherical and chromatic aberration of the electron-optical lens system and techniques like STEM have proven to give a new insight into atomic resolution structure determination. By HAADF-STEM and EELS mapping, we confirm in this work the layered-type ordering of Gd and Ba in the $GdBaMnFeO_{6-\delta}$ perovskite. Besides, we obtain information of the location of the anion vacancies by means of digital exit surface wave reconstruction (EWR) processing of focal image series. When this technique is used in combination with the hardware correction of the spherical aberration, better resolution limit than the point resolution of the microscope is achieved directly from the images [15]. This allows identification of the light oxygen atoms in the phase image of the exit wave and by structure modelling and quantum-mechanical simulations of the electron scattering process is possible to quantify the oxygen occupancy column by column of the anion sublattice. We have recently used EWR to locate the anion vacancies within the anion sublattice in the $GdBaMn_2O_{5.75}$ perovskite [16]. In this current work, we have located the anion vacancies within the $(GdO)_x$ planes in the crystal structure of the $GdBaMnFeO_{6-\delta}$ perovskite.

Experimental

$Gd_{0.5}Ba_{0.5}Mn_{0.5}Fe_{0.5}O_{3-\delta}$ and $GdBaMnFeO_{6-\delta}$ have been prepared by solid-state reaction using Gd_2O_3 (Sigma Aldrich, 99.99%), $BaCO_3$ (Sigma Aldrich, 99.99%), Mn_2O_3 (Sigma Aldrich, 99.99%) and Fe_2O_3 (Sigma Aldrich, 99.99%). Gd_2O_3 was heated at 900 ºC and $BaCO_3$, Mn_2O_3, Fe_2O_3 at 200 ºC prior to weighing. Stoichiometric amounts of the starting compounds were ground together and heated at 1000 ºC for 12 hours for

decarbonation in air. Afterwards, the samples were again grounded, pelleted and then either fired at 1400 ºC in air and slowly cooled in the furnace at 2 ºC/min. After this treatment, some samples were heated at 675 ºC in H_2/N_2 flow (%H_2 < 5.7%) during 4 hours and slowly cooled for promoting the Ba and Gd ordering. After the annealing in H_2/N_2 also some samples were treated at 550 ºC in O_2 flow for 10 hours.

Crystalline phase identification has been carried out by X-ray powder diffraction (XRPD) using a PANalytical X'PERT PRO MPD diffractometer with Cu $K_{\alpha 1}$ radiation and X'PERT PEAPD software. The patterns were taken at step mode with a step size equal to 0.02 (2θ degrees) and time per step equal to 10 s.

For transmission electron microscopy studies the samples have been ground in *n*-butyl alcohol and ultrasonically dispersed. A few drops of the resulting suspension were deposited in a carbon-coated grid. SAED, HRTEM, EELS and EWR experiments have been performed with a JEOL JEM 3000F microscope operating at 300 kV (double tilt (±20º) (point resolution 0.17 nm), fitted with a XEDS microanalysis system (OXFORD INCA) and ENFINA spectrometer with an energy resolution of 1.3 eV. The atomic ratio of the metals has been determined by X-ray energy dispersive spectroscopy (XEDS) analyses finding good agreement between analytical and nominal composition in all the crystals. Average oxidation state of Mn and Fe atoms and therefore oxygen content of the samples has been determined by EELS. The spectra were acquired in diffraction mode, with a dispersion of 0.1 eV px^{-1}, a collection angle β = 3.3 mrad and an acquisition time of 2 s. The background of all the raw spectra was removed using a power-law model. When necessary, plural-scattering effects were removed with a Fourier-ratio deconvolution method [17]. Focus series of twenty images were recorded with a focal increment of 3 nm starting from –144 nm. The exit-plane wave was reconstructed and residual aberrations were numerically corrected for the complex valued exit-plane wave using the IWFR software, [18] reaching the information limit of the JEM 3000F microscope (0.11 nm). High Angle Annular Dark Field Scanning Transmission Electron Microscopy (HAADF-STEM) experiments have been carried out in a JEOL JEM ARM 200cF with aberration correction of the condense lens giving a point resolution of 0.08 nm in STEM mode.

Thermogravimetric analysis (TGA)have been carried out in air to evaluate oxygen stoichiometry stability of the samples from 25 ºC to 900 ºC in heating and cooling rate.

Area specific resistance (ASR) associated to the electrode polarisation process at different temperatures has been determined by AC impedance spectroscopy on symmetrical two-electrode cells. The impedance measurements were carried out using a frequency response analyzer Solartron 1255A with a dielectric interface 1296. Measurements were performed in air on heating and cooling cycles between 500 ºC and 700 ºC, in a frequency range of 0.1 Hz to 1 MHz and an excitation voltage of 50 mV. Electrolyte pellets of 10 mm diameter and 1.2 mm thickness of commercial $Ce_{0.9}Gd_{0.1}O_{2-\delta}$ (CGO) powder (Fuel Cells Materials) were prepared by pressing the powder at 250 MPa and sintering in air at 1400ºC for 12 hours. A slurry prepared by $GdBaMnFeO_{6-\delta}$:CGO and $Gd_{0.5}Ba_{0.5}Mn_{0.5}Fe_{0.5}O_{3-\delta}$:CGO composites (70:30 wt %) with a commercial organic vehicle (Decoflux™) was deposited onto both surfaces of the CGO electrolyte and then fired at 900 ºC for 3 h in air (heating/cooling rate of 2.5 ºC min^{-1}). Silver paste and mesh were used as current collectors on both sides of the pellets. The impedance spectra were fitted to equivalent circuits using the Zview software [19]. Chemical stability of the materials with the CGO was proven prior to the electrochemical studies.

Results and Discussion

Fig. 1 SI shows the XRPD patterns at room temperature of the oxides prepared under different conditions. Single phase materials were obtained in all cases. The pattern of the compound prepared in air is characteristic of cubic perovskite structure. The patterns of the compounds prepared in H_2/N_2 show splitting of some reflections and extra reflections. These patterns can be indexed with an $a_p \times a_p \times 2a_p$ superlattice (a_p refers to the cubic perovskite structure).

Fig. 1 shows the SAED patterns along the $[010]_p$ and $[-110]_p$ zone axes of a crystal of the material prepared in air (Fig. 1a and b); of a crystal of the material prepared in H_2/N_2 (Fig. 1c and d) and the HRTEM images corresponding to the $[-110]_p$ zone axis of both compounds (Fig. 1e and f). The materials prepared in H_2/N_2 and afterwards annealed in O_2 have similar SAED patterns and HRTEM images than those of the material only heated in H_2/N_2. The SAED patterns have been indexed according to the cubic perovskite structure. The patterns and the HRTEM images of the oxide prepared in air do not show clear evidence of layered-type ordering of the Ba and Gd cations: there are

not extra reflections associated to doubling of the c-lattice parameter and the contrast differences of the HRTEM image do not indicate a $2a_p$ periodicity along the $[001]_p$ direction. However, there are weak extra reflections at $G_p \pm ½ (111)^*_p$ probably related to tilting of the AO_6 octahedra network [20] and a weak diffuse scattering along the $[001]_p$ direction probably associated to a partial ordering effect in local nano-domains. On the contrary, in the patterns of Fig. 1c and d, in addition to the Bragg reflections of the perovskite structure, there are strong superlattice reflections at $G_p \pm ½ (001)^*_p$ and the HRTEM image in Fig. 1f shows contrast differences indicating a $2a_p$ periodicity along the $[001]_p$ direction. These superlattice reflections and the $2a_p$ periodicity along the $[001]_p$ direction deduced from the HRTEM images are most probably associated to the layered-type ordering of the Ba and Gd atoms, which is confirmed by HAADF-STEM experiments in combination with EELS analysis. Therefore, the oxide prepared in air does not have A-cation ordering and from now it will be named $Gd_{0.5}Ba_{0.5}Mn_{0.5}Fe_{0.5}O_{3-\delta}$ but the compounds prepared in H_2/N_2 have layered-type ordering of Ba and Gd and are named $GdBaMnFeO_{6-\delta}$. At this point, it is worth mentioning that all the HRTEM images of crystals of $GdBaMnFeO_{6-\delta}$ show the existence of defects (indicated by yellow arrows in Fig. 1f) in the layer-stacking along the $[001]_p$ direction of the crystal structure. These defects and local disordering in some domains are also evidenced in the streaking along $[001]_p$ observed in the SAED patterns.

Fig. 2 a and b shows the HAADF-STEM images along the $[010]_p$ and $[-110]_p$ zone axes of a crystal of $GdBaMnFeO_{6-\delta}$. The contrast distribution in the images indicates that the cations are ordered in (001) layers along $[001]_p$ causing a $2a_p$ periodicity of the crystal structure along this direction. The line intensity profiles over $[001]_p$ (Fig. 2c and d) also show a 0.8 nm ($2a_p$) periodicity in the contrast intensity variation. Fig. 2SI shows a typical EELS spectrum of $GdBaMnFeO_{6-\delta}$. The variation of intensity of the Ba-$M_{4,5}$ and Gd-$M_{4,5}$ edge signals, obtained from the HAAD-STEM-EELS line scan along $[001]_p$ (Fig. 3) shows that (001) layers of Gd atoms (highest contrast intensity layers) alternate with (001) layers of Ba atoms (lower contrast intensity layers) with 0.8 nm separation between layers of similar kind of atoms. Therefore, these results confirm the layered-type ordering of Ba and Gd atoms along the $[001]_p$ direction of the crystal structure of the $GdBaMnFeO_{6-\delta}$ oxide.

The HAADF-STEM images also show clear evidence of layer-stacking defects in the crystals (indicated by yellow arrows in Fig. 2a). Fig. 3 SI shows two HAADF-STEM images along the $[010]_p$ zone axis of a crystal of $GdBaMnFeO_{6-\delta}$ with defects. In some areas of the crystal, two consecutive brighter layers appear indicating alteration of the stacking sequence of the A-cation layers. Two consecutive layers of Gd form the stacking defect, as it is also demonstrated by elemental EELS mapping. Fig. 4 shows the Ba-$M_{4,5}$ and Gd-$M_{4,5}$ map of two areas of a crystal, one without defects, in which Ba and Gd atoms alternate (Fig. 4a) and one area with a defect which consists of two consecutive Gd layers (Fig. 4b). A close inspection of the stacking defect reveals that the Gd atoms are shifted by $(1/2\ 0\ 0)_p$ along the $[100]_p$ direction. This defect layers resemble to the AO rock-salt-type layer of the K_2NiF_4-type structure. The presence of a significant number of layer-stacking defects (alteration of the stacking sequence of the A-cation layers due to existence of two consecutive layers of Gd) would modify the A-cation stoichiometry of the materials. However, the XEDS analysis carried out in the sample in a significant number of particles indicates good agreement between analytical and nominal composition in all the crystals. Therefore, there must be some A-cation layers with slightly extra amount of Ba-atoms that cannot be detected by HAADF-STEM and probably located in those domains of the crystal with no perfect layered ordering.

Determination of the oxygen content and location of the anion vacancies are essential to understand the conducting properties of these materials. EELS experiments have been carried out to evaluate the oxidation state of Mn and Fe and therefore the oxygen stoichiometry of the compounds. We have used four Mn oxides and three Fe oxides as standards to build up the corresponding graphic representations of the L_3/L_2 intensity ratio of the cation vs oxidation state (Fig. 4a and b SI). Following the procedure reported by Schmid and Mader [21] the average oxidation state of Mn in the oxides is obtained by interpolation of the Mn-L_3/L_2 intensity ratio determined acquiring spectra from 10 different crystals in the curve in Fig. 4a SI and the average oxidation state of Fe in the oxides is obtained by interpolation of the Fe-L_3/L_2 intensity ratio determined acquiring spectra from 10 different crystals in the curve in Fig. 4b SI. Table 1 summarizes the average oxidation state of Mn and Fe and the oxygen content of the compounds prepared under different conditions. All the oxides present non-stoichiometry in the anion sublattice.

Anion vacancies are expected to be located within the $(GdO)_x$ planes in the oxides with layered-type ordering of Ba and Gd. We have performed an exit wave reconstruction (EWR) experiment for obtaining information of the preferred location of the oxygen vacancies in the$GdBaMnFeO_{5.52}$ oxide. The most appropriate projection for this analyses is along the $[010]_p$ zone, where we expect to image columns of oxygen atoms (and vacancies) in the $(GdO)_x$ planes as it has been previously reported for $GdBaMn_2O_{5.75}$ [16]. A focal series of 20 images with an equidistant focal decrease was recorded along the $[010]_p$ zone axis using a slow-scan CCD camera. The reconstruction and numerical correction for the aberrations were performed using the IWFR software. The amplitude and phase images of the reconstructed exit wave are presented in Fig 5 SI. The Fast Fourier Transform of the image indicates that the limit resolution of the microscope (0.11 nm) has been reached.

In the phase image, the bright contrasts are located at the atom positions. In addition to the strong Ba/Gd and Fe/Mn signals, weak contrasts arising from the oxygen columns are clearly resolved, allowing to identify the different atomic columns whithin the projected structural model overlapping the experimental image (see Fig. 5). The intensity profile along the $[001]_p$ direction of the row marked by red arrows in Figure 5a clearly reproduces the ordering of Gd and Ba along $[001]_p$ with the intensity maxima belonging to the Gd slightly higher, in agreement with the atomic arrangement detected in the HAAD-STEM images and with the oxygen peaks showing almost a similar intensity (upper graph of Fig. 5b). However, in the profile (shown at the bottom of Fig. 5b) of the row of Fe/Mn-O columns running along the $[100]_p$ direction, the peaks with higher intensity correspond to the Mn/Fe columns, whereas the peaks belonging to the O columns exhibit a weaker intensity and vary regularly, with lower intensity in those columns located near the Gd atomic columns and higher when the closest atom is Ba, indicating a concentration of the oxygen vacancies in those positions closer to Gd.

Variations of the oxygen content of the materials with the temperature give place to variations of the crystal lattice volume that can limit their use as electrodes in SOFCs. Fig. 5 SI shows thermogravimetric curves taken in air of the three samples indicated in Table 1. Variation of the oxygen content with temperature is also represented in the graphics taken as initial content the one determined by EELS. The materials do not have significant variations of the oxygen content with the temperature except the oxide prepared in H_2/N_2, which suffers an important mass increase at about 200 ºC upon heating, followed by a slight mass decrease from 200 ºC to 900ºC and a slight increase

upon cooling. However, this oxide does not have important variations of the oxygen content in further heating-cooling cycles and therefore, presents similar thermal behaviour upon performance of the SOFC than the other materials studied. The oxygen content of the perovskites after one heating-cooling cycle is also indicated in Table 1. Fig. 6a shows complex impedance diagrams of symmetrical cells based on $GdBaMnFeO_{5.55}$ and $Gd_{0.5}Ba_{0.5}Mn_{0.5}Fe_{0.5}O_{2.78}$ as electrode materials with $Ce_{0.9}Gd_{0.1}O_{2-\delta}$ electrolyte recorded in air at 650 ºC and Fig. 6b shows the ASR values associated to the overall electrode polarization processes. The ASR values have been determined from raw impedance spectra taking into the account the high and low-frequency x-axis intercepts. The impedance spectra were fitted to equivalent circuits using the equivalent circuit indicated in the inset, in which the electrode process displays two major contributions, at intermediate and low frequencies [22-24]. In order to separate the different contributions, the impedance spectra have been fitted to a series circuit, based on an inductance (L) caused by the electrochemical setup, an ohmic resistance, (Rs) mainly, associated to the total ion transport in the electrolyte and two parallel RQ circuits associated to processes at the electrolyte-electrode interface and at the electrode surface, taking place at intermediate and low frequencies respectively. Similar ASR values are obtained on both heating and cooling cycles. Lower ASR values are obtained with $GdBaMnFeO_{5.52}$ than with $Gd_{0.5}Ba_{0.5}Mn_{0.5}Fe_{0.5}O_{2.78}$ in the whole range of temperature. We find that layered-type $GdBaMnFeO_{6-\delta}$ perovskites show better electrode performance for symmetric cells than disordered $Gd_{0.5}Ba_{0.5}Mn_{0.5}Fe_{0.5}O_{3-\delta}$.

Conclusions

Layered-type ordering is achieved in $GdBaMnFeO_{6-\delta}$ perovskites by annealing in H_2/N_2 at 675 ºC in one of the steps of the synthesis method. However, the crystals always show a relatively high concentration of layer-stacking defects. A combination of TEM techniques has allowed confirming this type of A-cation ordering. SAED and HRTEM suggest a modulation of the crystal structure giving a $2a_p$ periodicity along the $[001]_p$ associated to layered-type ordering of cations. Ba and Gd ordering in $(001)_p$ layers is confirmed by HAAD-STEM and EELS scans and mapping, which also demonstrate that the stacking defects consists of GdO planes. In addition to the layered-type ordering,

location of the anion vacancies within the $(GdO)_x$ layers of the crystal structure is concluded from EWR experiments, reconstructing a phase image along the $[010]_p$ zone axis. Analysis of the intensity of the averaged phase image reveals columns with lower occupation of oxygen atoms in the $(GdO)_x$ planes.

Layered-type ordered $GdBaMnFeO_{6-\delta}$ and disordered $Gd_{0.5}Ba_{0.5}Mn_{0.5}Fe_{0.5}O_{3-\delta}$ perovskites have been tested as cathodes in symmetrical cells using $Ce_{0.9}Gd_{0.1}O_{2-\delta}$ electrolyte. Lower ASR values are observed in the cells using $GdBaMnFeO_{6-\delta}$ electrodes. However, high ASR values are observed in these perovskites compared to $GdBaCo_2O_{6-\delta}$ [24], which limit their use in IT-SOFCs, but lower thermal expansion coefficients are expected. Improvement of the electrochemical behaviour might be possible by optimization of the synthesis method to obtain complete long range ordered layered-type perovskites with non-stacking defects. These results are in agreement with those reported by Taskin et al., [3, 4] which suggest that oxygen diffusion is significantly higher in layered-type perovskites in comparison with the corresponding cation disordered oxides and therefore show better electrochemical properties as electrodes in SOFCs.

Acknowledgements

Authors thank the Spanish MINECO for funding projects MAT2013-46452-C4-4-R, PIB2010JP-00181 and CAM for project MATERYENER3CM-S2013/MIT-2753. We thank the ICTS-Centro Nacional de Microscopía Electrónica de la U.C.M. for technical assistance.

References

[1] A. Aguadero, L. Fawcett, S. Taub, R. Woolley, K. T. Wu, N. Xu, J. A. Kilner and S. J. Skinner, J. Mater. Sci., 2012, **47**, 3925-3948.

[2] E. Kendrick, P. R. Slater, Annu. Rep. Prog. Chem., Sect. A: Inorg. Chem 2013, **109**, 396-420.

[3] A. A. Taskin , A. N. Lavrov , A. Yoichi , Appl. Phys. Lett. 2005, **86**, 091910 .

[4] A. A. Taskin , A. N. Lavrov , A. Yoichi , Prog. Solid State Chem. 2007, **35**, 481.

[5] D. Parfitt, A. Chroneos, A. Tarancón and J. A. Kilner, J. Mater. Chem. 2011, **21**, 2183-2186.

[6] M. Burriel, J. Peña-Martínez, R.J. Chater, S. Fearn, A.V. Berenov, S.J. Skinner, J. A. Kilner, Chem. Mater. 2012, **24**, 613-621.

[7] A. Chang, S. J. Skinner and J. A. Kilner, Solid State Ionics. 2006, **177**, 2009-2011.

[8] A. Tarancon, S. J. Skinner, R. J. Chater, F. Hernández-Ramírez and J. A. Kilner, J. Mater. Chem. 2007, **17**, 3175-3181.

[9] C. Zhu, X. Liu, C. Yi, D. Yan, W. Su, J. Power Sources 2008, **185**, 193-196.

[10] Zhou, Q., He, T., Ji, Y. J. Power Sources 2008, **185**, 754.

[11] N.S. Tsvetkova, A. Yu. Zuev, D. S. Tsvetkov, J. Power Sources 2013, **243**, 403-408.

[12] D. S. Tsvetkov, I. L. Ivanov, D. A. Halyshkin, A. Yu Zuev, Dalton Trans. 2014, **43**, 11862-11866.

[13] S. Sengodan, S. Choi, A. Jun, T. H. Shin, Y-W Ju, H. Y. Jeong, J. Shin, J. T. S. Irvine, G. Kim. Nature Mater 2015, **14**, 205.

[14] F. Millange, V. Caignaert, B. Domengès, B. Raveau, Chem. Mater. 1998, **10**, 1974-1983.

[15] W. M. J. Coene , A. Thust , M. de Beeck , D. Van Dyck, Ultramicroscopy, 1996, **64**, 109-135.

[16] D. Ávila-Brande, G. King, E. Urones-Garrote, Subakti, A. Llobet, S. García-Martín, Adv. Funct. Mater. 2014, **24**, 2510–2517.

[17] R. F. Egerton , Electron Energy-Loss Spectroscopy in the Electron Microscope, 3rd ed. , Springer , New York , **2011** .

[18] IWFR, version 1.0; HREM Research Inc.: Higashimastuyama, Japan, Feb **2005.**

[19] Johnson D. ZView: A software Program for IES Analysis,Version 2.9c, Scribner Associates, Inc., 2005.

[20] D.Y. Woodward, I.M. Reany, Acta Crystallogr. B 2005, **61**, 387-399.

[21] H. K. Schmid , W. Mader , Micron, 2006, **37** , 426

[22] S. B. Adler, Solid State Ionics, 1998, **111**, 125-134.

[23] S. B. Adler, Chem. Rev., 2004, **104**, 4791-4843.

[24] D. Muñoz-Gil, D. Perez-Coll, J.Peña-Martinez, S. García-Martín, J. Power Sources 2014, **263**, 90-97

Figures:

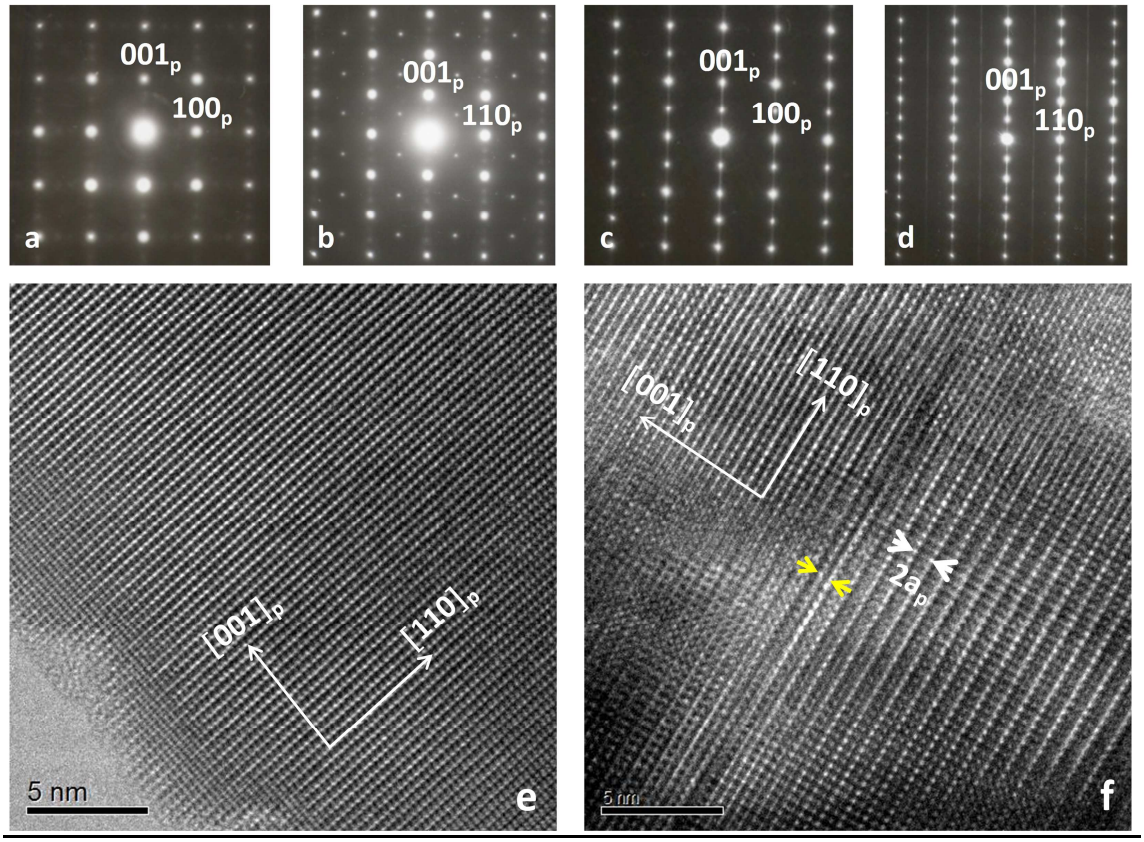

Fig. 1: SAED patterns of a $Gd_{0.5}Ba_{0.5}Mn_{0.5}Fe_{0.5}O_{3-\delta}$ crystal along the a) $[010]_p$ and b) $[-110]_p$, zone axes. SAED patterns of a $GdBaMnFeO_{6-\delta}$ crystal along the c) $[010]_p$ and d) $[-110]_p$, zone axes. HRTEM images recorded along the $[-110]_p$ zone axis of e) a $Gd_{0.5}Ba_{0.5}Mn_{0.5}Fe_{0.5}O_{3-\delta}$ crystal and f) a $GdBaMnFeO_{6-\delta}$ crystal.

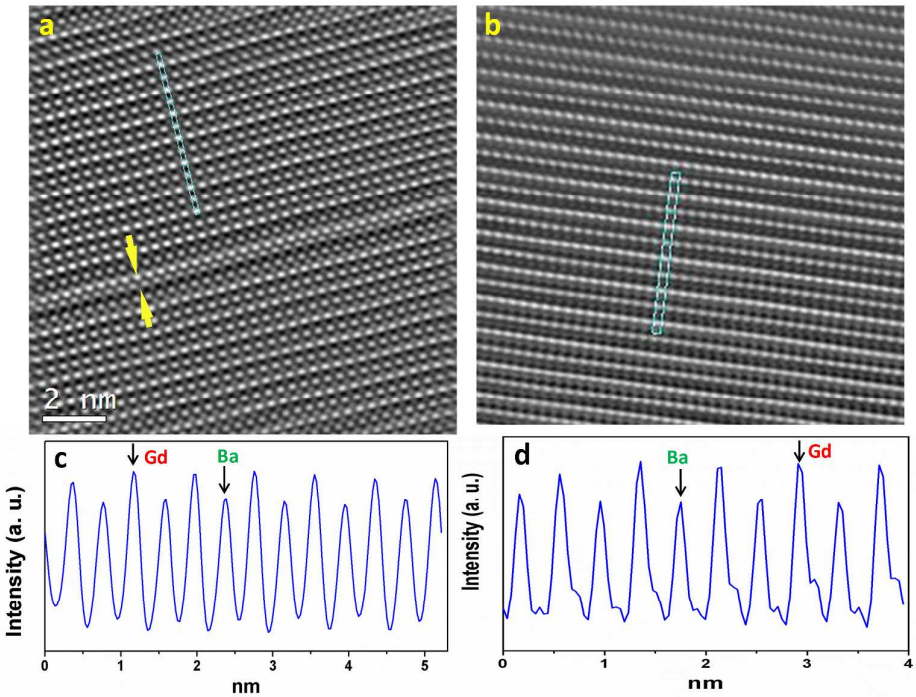

Fig. 2: Fourier-filtered HAADF-STEM images of a $GdBaMnFeO_{6-\delta}$ crystal along the a) $[010]_p$ and b) $[-110]_p$ zone axes. Line intensity profiles along $[001]_p$ of the images corresponding to the c) $[010]_p$ and d) $[-110]_p$, zone axes.

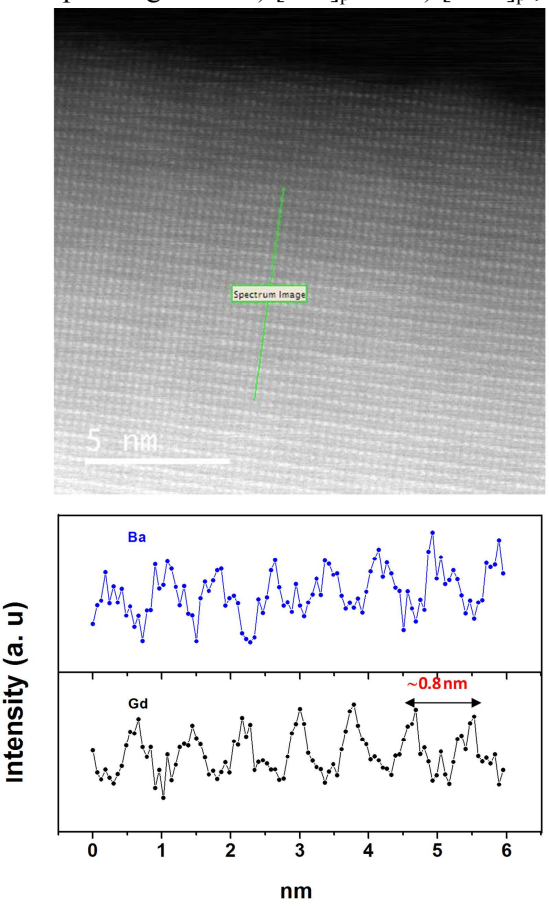

Fig. 3: Variation of intensity of the Ba-$M_{4,5}$ and Gd-$M_{4,5}$ edge signals, obtained from the EELS line scan along $[001]_p$ in an HAAD-STEM image of a $GdBaMnFeO_{6-\delta}$ crystal along the $[010]_p$ zone axis.

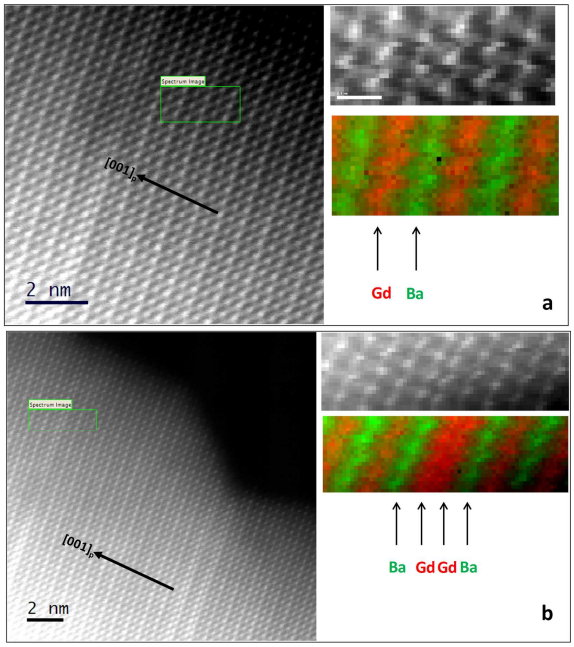

Fig. 4: Ba-$M_{4,5}$ and Gd-$M_{4,5}$ EELS maps of an area of a crystal of $GdBaMnFeO_{6-\delta}$ a) without defects and b) with defects. The areas are indicated in the corresponding HAADF-STEM image of the $[010]_p$ zone axis.

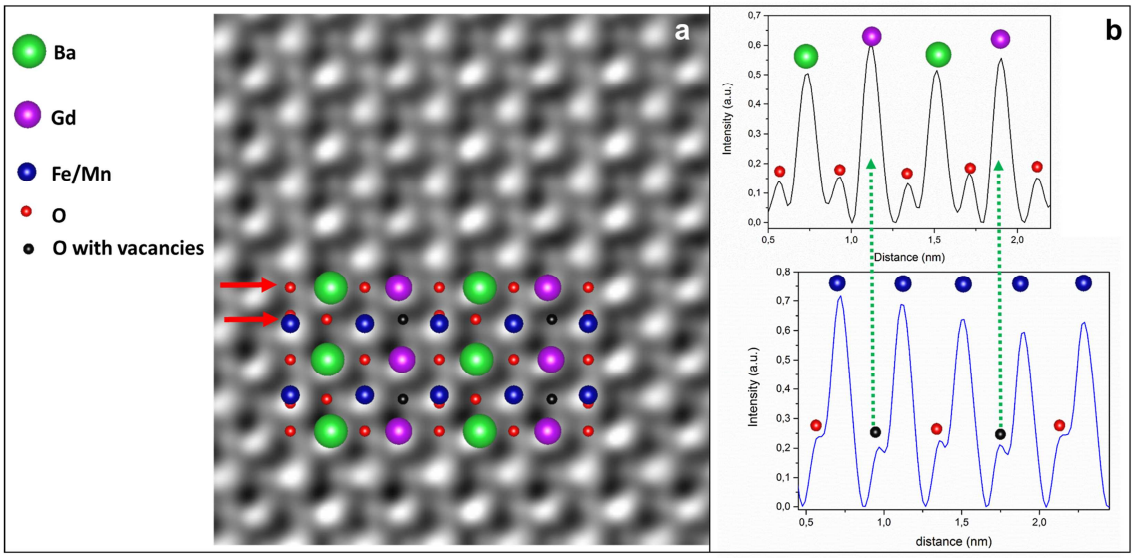

Fig. 5: a) Enlargement of the averaged phase image in Figure 5b SI. The bright dots correspond to the projected potential of the different atomic columns identified by the colors represented in the legend, b) Intensity profiles performed along the directions marked by red arrows in a). The green arrows indicate that the oxygen columns containing vacancies are located near the Gd atoms along $[100]_p$

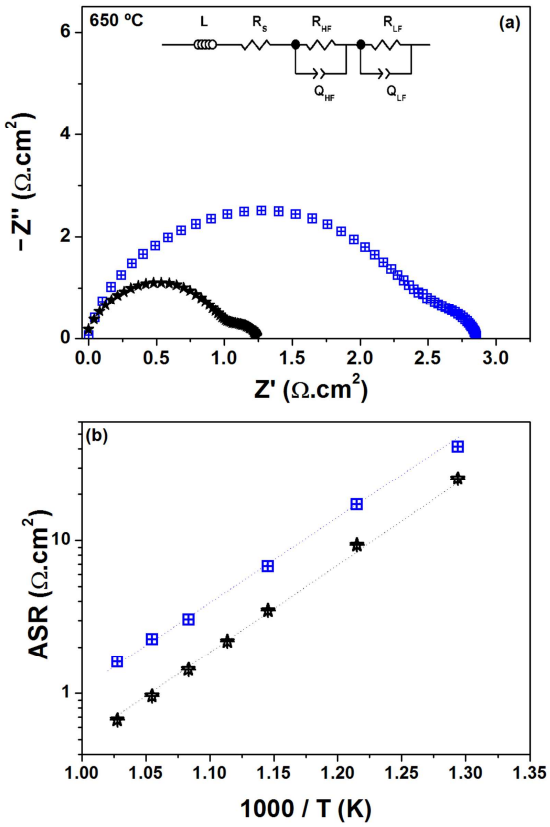

Fig. 6: a) Impedance spectra for symmetrical cells of $Gd_{0.5}Ba_{0.5}Mn_{0.5}Fe_{0.5}O_{2.78}$/CGO (blue) and $GdBaMnFeO_{5.55}$/CGO (black) at 650 °C in air. The equivalent circuit used for the fitting is represented in the inset. The impedance spectra have been shifted to x-axis origin for comparison; b) Arrhenius plot of the area-specific resistance (ASR) values, obtained from the impedance spectra of $Gd_{0.5}Ba_{0.5}Mn_{0.5}Fe_{0.5}O_{2.78}$/CGO (blue) and $GdBaMnFeO_{5.55}$/CGO (black) symmetrical cells.

Tables:

Table 1. Oxygen content of a sample prepared in air a); a sample prepared in H_2/N_2 b) and a sample prepared in H_2/N_2 and afterwards oxidized

Sample preparation	Oxygen content as prepared (EELS)	Oxygen content after TGA
Air	$Gd_{0.5}Ba_{0.5}Mn_{0.5}Fe_{0.5}O_{2.73}$	$Gd_{0.5}Ba_{0.5}Mn_{0.5}Fe_{0.5}O_{2.76}$
Air + H_2/N_2	$GdBaMnFeO_{5.10}$	$GdBaMnFeO_{5.55}$
H_2/N_2+O_2	$GdBaMnFeO_{5.52}$	$GdBaMnFeO_{5.58}$

Table of Contents:

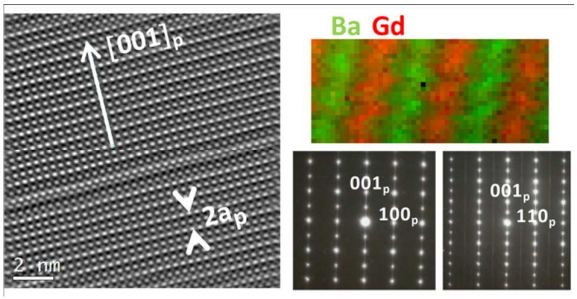

Layered-type ordering of Ba and Gd atoms in $BaGdMnFeO_{6-\delta}$ perovskite studied by HAADF-STEM and EELS mapping